Eco-Friendly Wood-Based Solid-State Flexible Supercapacitors from Wood Transverse Section Slice and Reduced Graphene Oxide

Shaoyi Lv,[1] Feng Fu,[1,*] Siqun Wang,[1,2] Jingda Huang,[1] and La Hu[1]

[1]Research Institute of Wood Industry, Chinese Academy of Forestry, Beijing 100091, China
[2]Center for Renewable Carbon, University of Tennessee, Knoxville, Tennessee, 37996, USA

An interesting wood-based all-solid-state supercapacitor is produced using reduced graphene oxide (RGO) coated on wood transverse section slice (WTSS) as electrode material by means of a low-cost, eco-friendly, and simple method for the first time. The RGO-coated WTSS electrode has a porous 3D honeycomb framework due to the hierarchical cellular structure of the WTSS substrate and can function as an electrolyte reservoir. This special construction endows this novel electrode with good areal capacitance (102 mF cm^{-2}) and excellent cyclic stability (capacitance retention of 98.9% after 5000 cycles). In addition, the supercapacitors exhibit good mechanical flexibility and preserve almost constant capacitive behavior under different bending conditions. Our study introduces a new and eco-friendly material design for electrodes in future flexible energy storage devices that closely resemble natural materials.

Keywords: wood slice, porous structure, flexible electrode, all-solid-state supercapacitor, reduced graphene oxide
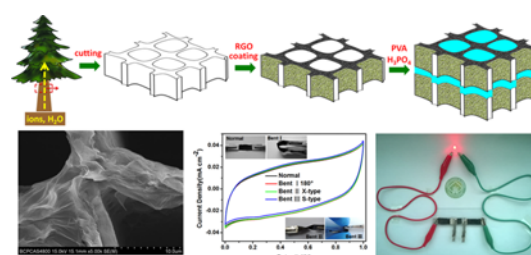
1. INTRODUCTION

Paper-based electrodes have been considered one of the most exciting new technologies for advancing the development of wearable and flexible equipment because of their low cost, light weight, environmental friendliness, and mechanical flexibility.[1-4] In this respect, intense interest recently has resulted in a significant number of research activities on cellulose/paper-based flexible supercapacitors.[5-8] Many nanostructured carbon materials, such as carbon nanotubes (CNTs) and graphene, can be easily attached to cellulose substrates to form freestanding and binder-free electrodes with outstanding flexibility for a large number of applications.[9-11] The cellulose substrates can provide excellent microporous structures and hydrophilic characteristics that have a positive effect on the electrochemical performance of supercapacitors.[12-14] Even though cellulose paper is considered to be a very environmentally friendly material, its production requires several chemical processes that are environmentally hazardous, particularly the separation from wood sources. Can natural wood be used directly as flexible

substrate in a "green" preparation process without transforming it first into cellulose paper? The answer is yes. Wood is cut along the radial direction to obtain transverse section slices at a thickness of less than 200 μm. The slices have good flexibility, excellent hydrophilic properties because of the presence of hydroxyl groups, and natural hierarchical cellular structures including microscale structures of cut cell walls.[15]

In this work, we use wood transverse section slice (WTSS) as flexible scaffold and reduced graphene oxide (RGO) as active material because of its excellent electrical conductivity and extremely large surface area, to create a surprisingly flexible electrode.[16] Only the transverse section of natural wood possesses a porous, 3D honeycomb framework.[17] This provides an even larger surface area than the radial and tangential section slices at the same thickness; as a result, high mass loading of RGO is enabled. In addition, the innate vessels and tracheids endow wood the ability to absorb various ions and water in the metabolic process. Therefore, WTSS can act as an ideal electrolyte reservoir. This property can increase the availability of the electrolyte and wettability of the WTSS-RGO electrode. The WTSS-RGO sheet is made of a flexible electrode material using an extremely simple and environmentally

friendly dipping and drying process. The RGO nanosheets are strongly attached to the WTSS and are distributed throughout its macroporous framework to form a conductive honeycomb network. The resulting wood-based supercapacitors showed good specific capacitance and excellent cyclability, which demonstrates that flexible supercapacitors based on the combination of WTSS and RGO are viable.

2. EXPERIMENTAL PROCEDURE

Graphite powder (C.P., Shanghai Chemical Reagent Co. Ltd.) and 85% aqueous solution of hydrazine hydrate (A.R., Beijing Chemical Reagent Co. Ltd.) were used without further purification. Native WTSSs of approximately 180 μm in thickness were cut from Chinese fir using rotary microtomy and subsequently vacuum dried at 50°C for 2 h. Aqueous dispersions of graphene oxide (GO) nanosheets were prepared from graphite powder using a modified Hummers's method.[18,19] The WTSSs were immersed in aqueous GO dispersions of 1 mg mL^{-1} for 5 min and dried naturally at room temperature. This procedure was repeated several times to achieve different GO loadings of 0.36 mg cm^{-2}, 0.49 mg cm^{-2}, and 0.68 mg cm^{-2}. Then, the WTSS-GO sheets were reduced by hydrazine hydrate at 90°C for 3 h. Finally, the resulting WTSS-RGO sheets were rinsed thoroughly with deionized water and vacuum dried at 50°C for 2 h. The supercapacitor was assembled in a traditional laminated two-electrode configuration, as shown in Fig. 1. PVA/H$_3$PO$_4$ gel was used as electrolyte and simultaneously as separator.

The microstructure was observed by scanning electron microscopy (SEM, Hitachi S-4800, JPN). The chemical element and functional groups were studied using X-ray photoelectron spectroscopy (XPS, PHI Quantera II, JPN) and Fourier-transform infrared spectroscopy (FTIR, Nicolet 6700, USA). The sheet resistance was measured using a 4-point probe resistivity measurement system (ST 2253, CHN). The mechanical strength was investigated using dynamical mechanical analysis (DMA, Physica MCR 301, GER). The electrochemical measurements were performed using a two-electrode test cell on a CHI 660E elec-

trochemical workstation (CH Instruments Inc.) at room temperature. The areal and gravimetric capacitance of the WTSS-RGO electrode was calculated according to $C_S = 4(\int IdV)/(vSV)$ and $C_g = 4(\int IdV)/(vmV)$ or $C_g = 4I\Delta t/(\Delta Vm)$, respectively, where I(A) is the current, v(V s^{-1}) the voltage sweep rate, V(V) the cell voltage, m(g) the total mass of the two symmetrical electrodes, and S(cm^2) is the geometrical area of the supercapacitor. The areal energy E(mWh cm^{-2}) and power P(mW cm^{-2}) of the WTSS-RGO supercapacitor were obtained according to $E = 1/4(C_S V^2/2)$ and $P = E/(V/v)$, respectively, where C_S, v, and V have been described above.

3. RESULTS AND DISCUSSION

The preparation process of native WTSS, WTSS-RGO electrode, and its supercapacitor is illustrated in Fig. 1. WTSS is the transverse section slice of wood tracheids. These fistulous slender cells can absorb and transport different types of ions and water and function as an ideal electrolyte reservoir. The porous 3D honeycomb structure of WTSS can effectively retain a hydrophilic ionic liquid in the WTSS-RGO matrix, which provides additional and continuous transport pathways through the active RGO and electrolyte phase, thereby improving the kinetics of ion transport. On the other hand, Chinese fir is a perennial softwood lumber with tracheids of relatively uniform pore size and pliable texture. It can be easily cut, yielding smooth sections and highly flexible wood slices. Furthermore, it has a specific surface area of 22.37 m^2 g^{-1} and porosity of 80.50%, as measured using mercury intrusion porosimetry (MIP) in our previous study.[20] The naturally porous 3D honeycomb structure provides favorable storage channels for the electrolyte and additional transportation corridors for ions.

The WTSS-RGO electrode was fabricated through a simple dipping-and-drying process. The flexible WTSS-RGO electrode can be bent up to 180 degrees very easily as it benefits from the high flexibility of WTSS, as shown in Fig. 2a. The morphological characteristics of WTSS before and after RGO coating were examined through SEM. The transverse, radial, and tangential section slices are shown in Fig. 2b, 2c, and 2d, respectively. It can be clearly seen that
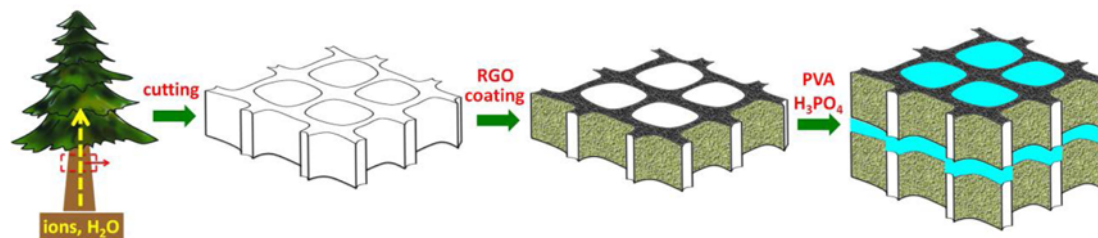
Fig. 1. Schematic diagram of the preparation processes of native WTSS, WTSS-RGO, and its supercapacitor. Both black and green textures represent RGO coating. Different colors are used to distinguish different cross sections. The pure blue texture indicates the PVA/H$_3$PO$_4$ gel electrolyte.
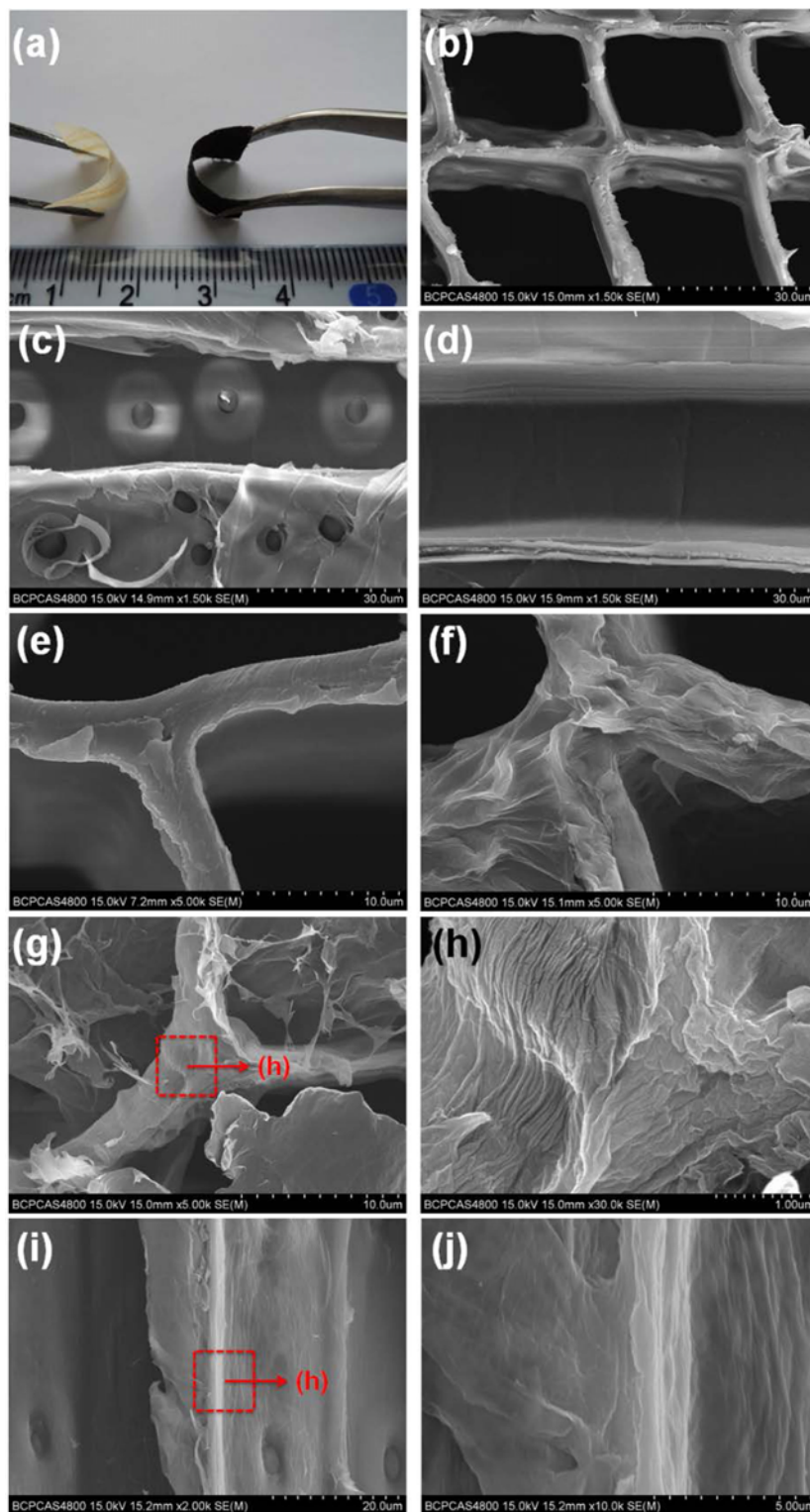
Fig. 2. (a) Representative photographs of WTSS and WTSS-RGO electrodes demonstrating their flexibility. (b), (c), and (d) SEM images at identical magnification of transverse, radial, and tangential section slices, respectively. (e) SEM image of WTSS at higher magnification. (f) SEM image of the WTSS-RGO electrode at the RGO loading of 0.36 mg cm^{-2} at the same magnification of frame (e). (g) High-resolution (similar to images (e) and (f)) SEM image of the WTSS-RGO electrode at the RGO loading of 0.49 mg cm^{-2}. (h) SEM image of the WTSS-RGO electrode at enlarged scale corresponding to the red-marked frame in image (g) showing wrinkled textures. (i) and (j) Cross-sectional SEM images of the WTSS-RGO electrode at the RGO loading of 0.68 mg cm^{-2} at different scales; (j) shows the wrinkled textures of the inner wall surface of the tracheid cell wall at larger magnification corresponding to the red-marked frame in image (i).

the transverse section slice shows the transversal tracheid structure while the radial and tangential section slices reveal the longitudinal tracheid profile. The round orifices in Fig. 2c are the pits. Therefore, the porous 3D honeycomb structure can be identified only in the WTSS. Both the section and inner wall surface of the tracheid cell wall appear to be very smooth (Fig. 2e). However, after RGO is deposited onto WTSS, RGO nanosheets can be observed inside the porous structure (Fig. 2g). The surface of the tracheid cell wall is no longer smooth, and an RGO layer is clearly observed adhering onto the cell wall (Fig. 2f). The RGO layer attached to the tracheid cell wall has a rougher and more wrinkled texture than the RGO nanosheets in the porous structure, as shown in Fig. 2h.[5] The wrinkled textures also appear at the inner wall surface of the tracheid cell wall, as shown in the cross-sectional images of WTSS-RGO in Fig. 2g and 2i. This indicates that the RGO layer is attached to the entire surface of the porous 3D honeycomb framework of the WTSS. In addition, no apparent interface can be observed between wood and attached RGO layer in the cross-sectional image Fig. 2j, indicating strong adhesion between them. This strong adhesion may be ascribed to strong hydrogen bonding between the hydroxyl groups of the wood and hydroxyl or carboxyl groups of the RGO nanosheets.[10] Further, this strong adhesion guarantees good mechanical stability of the WTSS-RGO electrode during bending.

As the dipping-and-drying process is repeated many times, the tracheid cell-wall surfaces and the voids in the porous honeycombed framework of WTSS are gradually covered and filled with RGO, leading to increased mass loading of RGO and morphological changes of the microstructure of the WTSS-RGO electrode. It can be observed in Fig. 3a-c that the honeycomb pores of the WTSS are gradually covered by RGO, with increasing RGO loading from 0.36 to 0.68 mg cm^{-2}. At enlarged magnification, Fig. 3d-f further demonstrates that the RGO nanosheets are first attached to the surfaces of the tracheid cell wall, then form a discontinuous lamellar structure inside the honeycomb pores (Fig. 3e), and finally, these lamellar RGO nanosheets are connected to each other to form a continuous sheet as a result of the dense packing of the RGO nanosheets using π-π stacking (Fig. 3f).[21,22] The porous structure of the WTSS is not clogged by these lamellar RGO nanosheets, ensuring its functionality as an electrolyte reservoir.

XPS can be used to examine the surface elemental composition before and after the RGO coating. As evident from Fig. 4a, pronounced C 1s and O 1s peaks are observed at binding energies of approximately 284 and 532 eV, respectively, and the proportions of carbon and oxygen changed upon coating with GO and RGO. High-resolution XPS C 1s spectra of WTSS, WTSS-GO, and WTSS-RGO are shown in Fig. 4b-d, respectively. The curves can be deconvoluted into four individual contributions arising from carbon functional groups, namely C=C/C-C (284.8 eV), C-O (286.9 eV), C=O (288.4 eV), O-C=O (289.8 eV) for WTSS-GO and C=C/C-C (284.8 eV), C-O (286.1 eV), C=O (287.0 eV), O-C=O (288.5 eV) for WTSS-RGO.[23] The C-O peak intensity of WTSS-RGO obviously decreases compared with that of WTSS-GO. This indicates that the GO nanosheets are effectively reduced by hydrazine hydrate,[24] which can also be proven by the C/O ratio of WTSS-GO, which increases at approximate values from 2.60 to 5.51 after reduction (inset of Fig. 4a). The FTIR
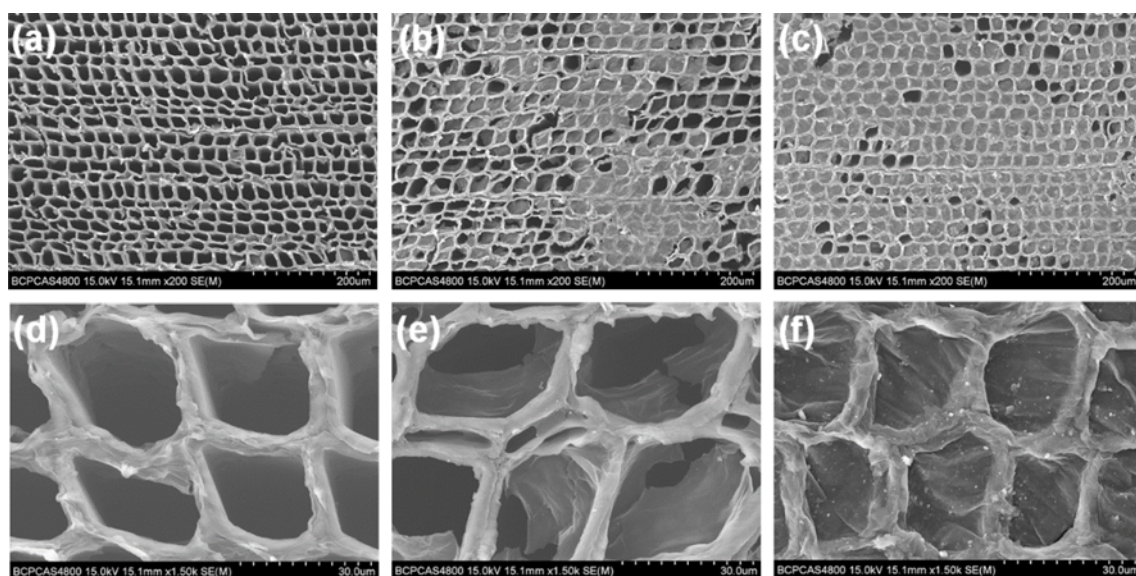
Fig. 3. (a), (b), and (c): SEM images of the surface morphology of WTSS-RGO electrodes at different RGO loadings of 0.36, 0.49, and 0.68 mg cm^{-2}. (d), (e), and (f): Details at enlarged scale of (a), (b), and (c) respectively.
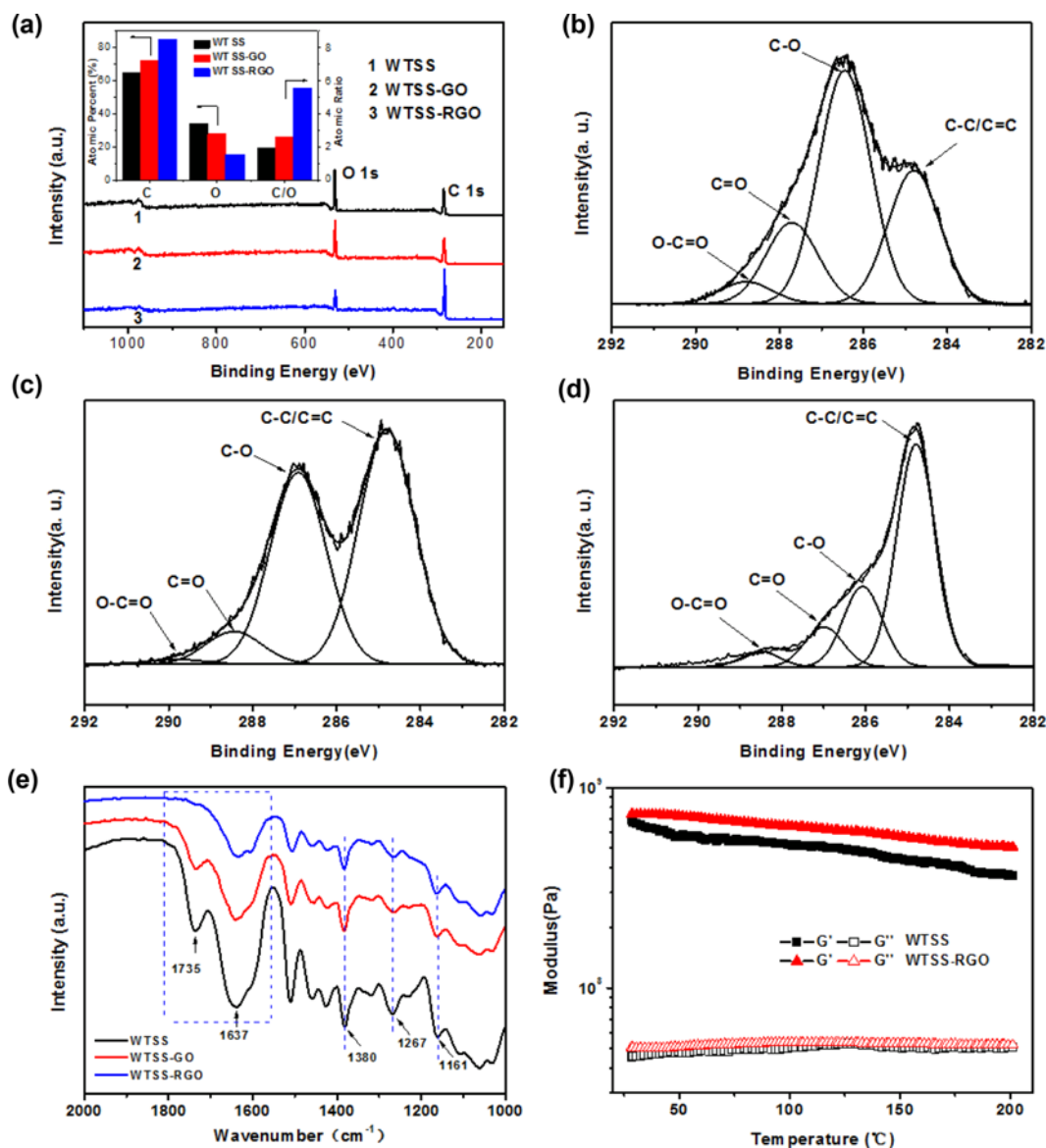
Fig. 4. (a) XPS wide-region survey spectra of WTSS, WTSS-GO, and WTSS-RGO. The inset shows the deduced elemental percentages and C/O ratios of WTSS, WTSS-GO, and WTSS-RGO. High-resolution XPS C1 spectra of (b) WTSS, (c) WTSS-GO, and (d) WTSS-RGO. (e) FTIR spectra of WTSS, WTSS-GO, and WTSS-RGO. (f) Dynamic mechanical behavior of WTSS and WTSS-RGO at the RGO loading of 0.68 mg cm^{-2}.

spectra of WTSS, WTSS-GO, and WTSS-RGO (Fig. 4e), also show that after the reduction reaction, the C=O stretching (carboxyl/carbonyl) peak of WTSS-GO at 1735 cm^{-1} almost disappears. The C-OH stretching peak at 1637 cm^{-1}, the C-O stretching (carboxyl) peak at 1380 cm^{-1}, and the intensities at 1267 and 1161 cm^{-1} assigned to C-O-C and C-OH bonds, respectively, dramatically weaken, verifying that the GO nanosheets are reduced sufficiently.[25-27] These two types of spectroscopic results reflect the active materials RGO sheets, successfully attached to the walls of the porous-structured WTSS.

DMA tests were used to determine the mechanical strength of WTSS and WTSS-RGO, as shown in Fig. 4f. As the temperature increases from room temperature to 200°C, the storage moduli G' of the two samples decrease slowly, while the corresponding loss moduli G'' remains steady. The G' values of WTSS and WTSS-RGO are close to 10^9 Pa, reflecting high mechanical strength. Moreover, the mechanical strength of WTSS-RGO is slightly higher than that of WTSS, suggesting that RGO coating has a certain reinforcement effect on WTSS.

The electrochemical performance of the supercapacitors using WTSS-RGO electrodes with different RGO-loadings of 0.36, 0.49, and 0.68 mg cm^{-2} were examined using a two-
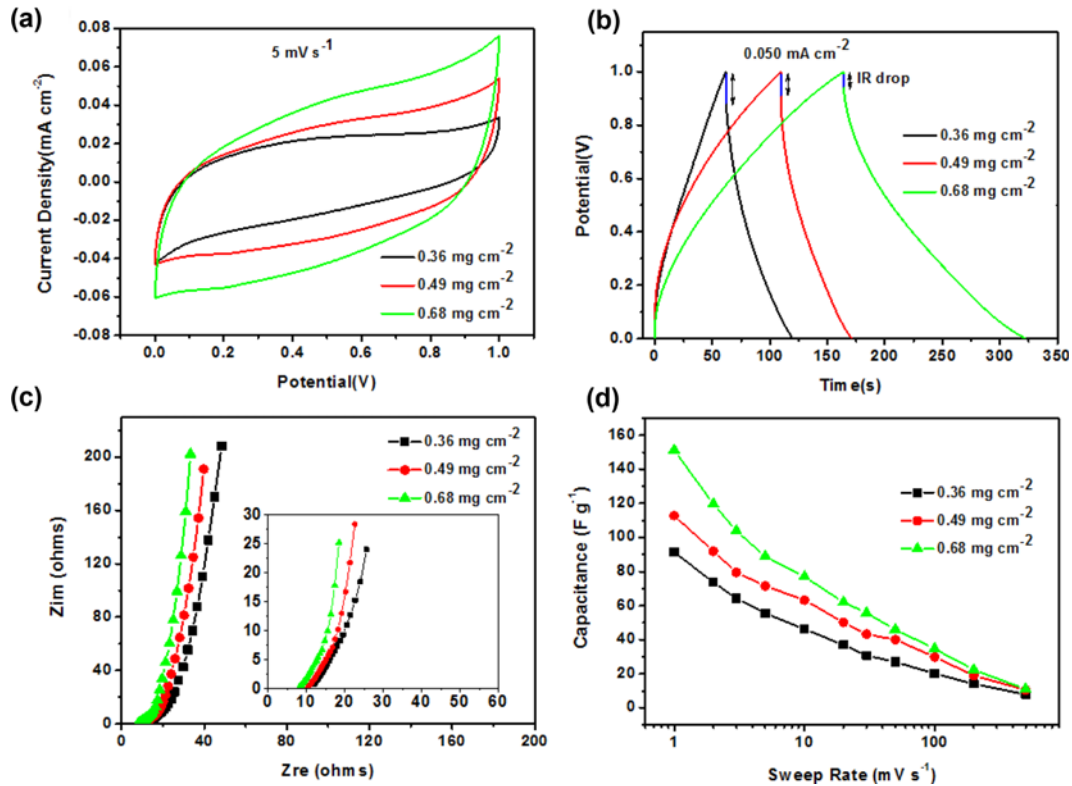
Fig. 5. (a) CV curves at the seep rate of 5 mV s^{-1}, (b) GCD curves at the current density of 0.05 mA cm^{-2}, and (c) EIS curves of supercapacitors using WTSS-RGO electrodes at RGO loadings of 0.36, 0.49, and 0.68 mg cm^{-2}. (d) Gravimetric capacitance of the WTSS-RGO electrode at RGO loadings of 0.36, 0.49, and 0.68 mg cm^{-2} at different sweep rate.

electrode test cell at room temperature (Fig. 5). Fig. 5a presents the cyclic voltammetry (CV) curves of the supercapacitor cells at a scan rate of 5 mV s^{-1} within the potential window from 0 to 1 V. All cells had similar rectangular-like shapes without any redox-current peaks indicating the typical capacitive behavior of an electrical double layer. With increasing RGO-loading, the enclosed area of the CV curves increased. Galvanostatic charge-discharge (GCD) studies of the supercapacitors were performed at cell voltages between 0 and 1.0 V at a discharge current density of 0.05 mA cm^{-2}, as shown in Fig. 5b. All charge-discharge curves have similar shape and reveal the typical pattern of carbon electrode-based cells with capacitive behavior. The GCD curves show decreased internal resistance (IR) drop during discharge with increased RGO loading, indicating enhanced conductivity of the WTSS-RGO electrode. Figure 5c shows the electro-chemical impedance spectroscopy (EIS) data in form of Nyquist plots for all investigated supercapacitor cells. From the magnified EIS spectra of the cells (Fig. 5c inset), the equivalent series resistance (written as R_s, including the intrinsic resistance of the electrode and the electrolyte resistivity) of the WTSS-RGO electrode with RGO loading of 0.36, 0.49, and 0.68 mg cm^{-2} is approximately 12, 10, and 8 Ω, respectively, obtained from the intercept of the Nyquist plot with the real axis.
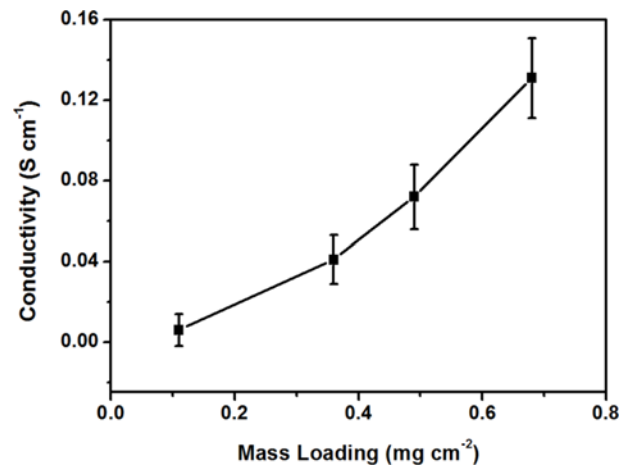

Fig. 6. Conductivity of WTSS-RGO with respect to RGO mass loading.

These results demonstrate that the enclosed area of the CV curves increases while the IR drop and R_s decrease on increasing RGO loading because the RGO nanosheets gradually form a continuous lamellar structure on the WTSS substrate, thereby increasing the conductivity of the WTSS-RGO electrodes. As shown in Fig. 6, the conductivity of the WTSS-RGO electrode with RGO loading of 0.36, 0.49, and

0.68 mg cm^{-2} is 0.04, 0.06, and 0.13 S cm^{-1}, respectively. This high conductivity ensures that the WTSS-RGO electrode can act as flexible current collector. Furthermore, larger RGO loading also leads to higher energy-storage capacity (Fig. 5d).[28,29] This result may be attributed to the effective ion migration in the WTSS-RGO electrodes, due to its porous 3D honeycomb structure and electrolyte reservoir (WTSS with adsorbed electrolyte). It should be noted here that the electrochemical performance of WTSS-RGO with RGO loading amount of 0.68 mg cm^{-2} is not the maximum. With respect to the confirmation of such a maximum, systematic design-of-experiment (DOE) studies are needed

and will be described in detail in a future study.

Details about the electrochemical performance of the supercapacitor with RGO loading of 0.68 mg cm^{-2} are shown in Fig. 7. A series of CV curves at different scan rates from 5 to 200 mV s^{-1} within the potential window from 0 to 1 V reveals the typical capacitive behavior of an electrical double layer (Fig. 7a). When the scan rate reaches 200 mV s^{-1}, the CV curve shows only little distortion. The areal capacitance of the WTSS-RGO electrode is 102 mF cm^{-2} or 151 F g^{-1} (based on the mass of RGO) at the scan rate of 1 mV s^{-1} (Fig. 7c and d). This specific capacitance is much higher than that of other RGO-based electrodes reported
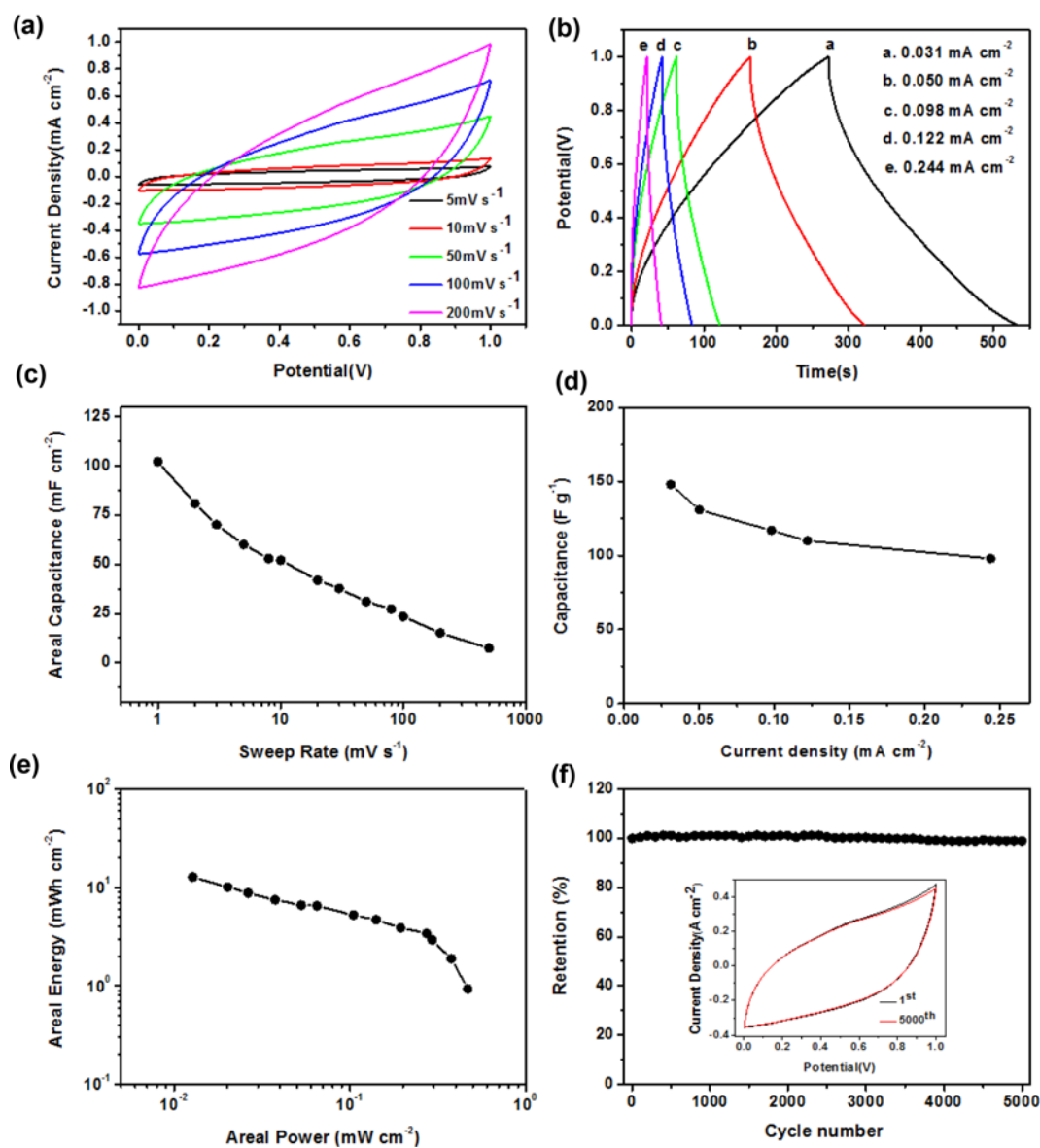
Fig. 7. (a) CV and (b) GCD curves of the WTSS-RGO supercapacitor. (c) Areal capacitance of the WTSS-RGO electrode at different sweep rates. (d) Gravimetric capacitance of the WTSS-RGO electrode against discharge current density. (e) Areal energy against areal power of the WTSS-RGO supercapacitor. The RGO loading is 0.68 mg cm^{-2}. (f) Cyclic stability of the WTSS-RGO supercapacitor measured at a sweep rate of 50 mV s^{-1}. The inset shows the CV curves of the 1st and 5000th cycle. The RGO loading is 0.68 mg cm^{-2}.

recently.[9,30] The performance of the present electrodes apparently benefits from the distinct porous 3D honeycomb structure and hydrophilic properties of WTSS.[31] Thus, the accessible surface area of RGO and migration efficiency of electrolyte ions are both improved.

The GCD studies of the flexible supercapacitor cell were performed with cutoff voltage of 0 - 1 V at different discharge current densities, as shown in Fig. 7b. The charge and discharge curves show a nearly symmetrical triangular shape, indicating good electrochemically capacitive behavior with less Faradaic reaction. Furthermore, the IR drop from the initial discharge phase is quite small, demonstrating that the supercapacitor cell has a relatively low series resistance. This is also confirmed by the EIS analysis of the super-capacitor with RGO loading of 0.68 mg cm^{-2} (Fig. 5c). In the high-frequency region (Fig. 5c inset), R_s reflected in the real-axis intercept is comparatively small, indicating good conductivity of the flexible WTSS-RGO electrode. The gravimetric capacitance can be estimated from the discharge curves (Fig. 7d). The value is about 148 F g^{-1} at the current density of 0.031 mA cm^{-2}. Even at the relatively high current density of 0.244 mA cm^{-2}, it still remains at a value of 98 F g^{-1} (66% of the initial capacitance), indicating that the WTSS-RGO electrode has good capacitance retention because of the porous 3D honeycomb structure of WTSS that acts as aqueous electrolyte reservoir, so the diffusion distance for the electrolyte ions is significantly reduced.[14]

As for the Ragone plot shown in Fig. 7e, the maximum areal energy of 12.77 mWh cm^{-2} and areal power of 0.47 mW cm^{-2} both are superior to previously reported results on paper substrates.[9] This high performance may be a result of the higher ion accessibility because of the high wettability of the WTSS-RGO electrode. The long-term cyclic stability of the assembled supercapacitor cell was examined using CV at the sweep rate of 50 mV s^{-1}, as shown in Fig. 7f. The capacitance barely decreased after 5000 cycles, and the retention retained the high value of 98.9%, which indicates

that this flexible supercapacitor cell had good cycling stability. The reason for this excellent performance may be that the pathway of electrolyte ions between the two electrodes is increased because of the porous 3D honeycomb structure of the WTSS-RGO electrode.

In order to further understand the flexibility of the device, the capacitive performance under various mechanical deformations was investigated by CV tests at the sweep rate of 2 mV s^{-1}. As evident from Fig. 8a, the three bent states (180°, X-type, and S-type) had almost no effect on the capacitive behavior of the flexible device. More strikingly, even under extreme bending (state III, S-type bending) the rectangular shape of the CV curve showed only very slight deformation. The flexible electrode under bending state III also had the areal capacitance of 80.3 F cm^{-2}, compared to 80.8 mF cm^{-2} of the normal state. The result indicates that the fabricated WTSS-RGO supercapacitor shows high flexibility and can be exploited in many types of commercial applications. This flexibility property can be traced to the fact that wood is a prominent natural composite material with fantastic inherent mechanical performance that plays an important role as framework for active materials. Additionally, Fig. 8b demonstrates that a red light-emitting diode (LED) can be operated by the device with three units in series, showing its high performance.

The electrochemical performance of a pesudocapacitor fabricated with natural porous wood slice and polypyrrole (PPy) was studied in our previous work.[32] Compared with the present study on porous electric double-layer capacitors composed of WTSS and RGO, the 3D honeycomb porous structure and hydrophilic characteristics of WTSS play an important role in the energy-storage capacitor and the performance of WTSS/PPy electrode is a little better than the WTSS-RGO electrode because of the more uniform distribution of the active material benefitting from the in situ polymerization.

The gravimetric capacitance of the presently investigated
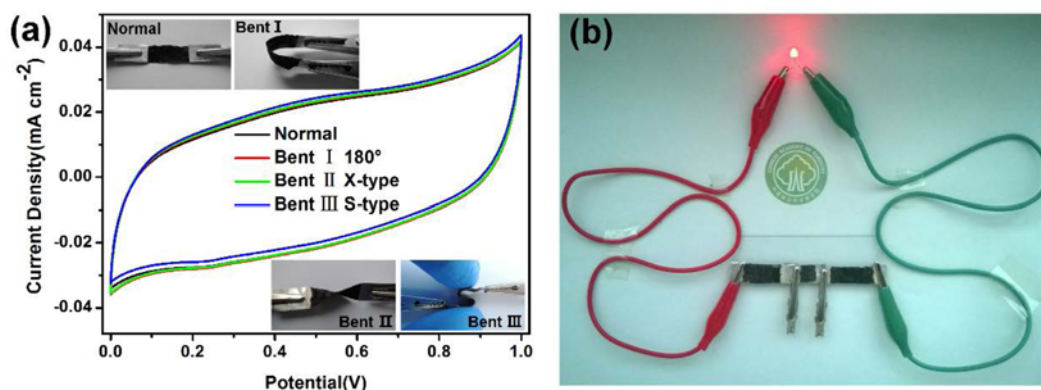
Fig. 8. (a) Comparison of the CV curves at 2 mV s^{-1} of the WTSS-RGO supercapacitor cell with an RGO loading of 0.68 mg cm^{-2} under normal and bent states. (b) Digital picture of a red LED operated by the fabricated supercapacitor cell with three units in series.

Table 1. Electrochemical performance of various scaffolds electrodes.

Scaffold	Active material	Capacitance (F g^{-1})	Reference
Cellulose paper	RGO	120	9
Cotton cloth	RGO	81.7	33
PET	RGO	118.5	34
Au-coated PET	RGO, Carbon black	112	35
Carbon-fiber cloth	RGO, PANI	1145	36
Wood slice	RGO	148	This paper

electrodes is compared in Table 1 with other electrodes based on various scaffolds reported in the literature. Obviously, the capacitance of our WTSS-based electrode is higher than that of cellulose paper, cotton cloth, and PET film-based electrodes reported in the literature,[9,33-35] except for the carbon fiber cloth-based RGO/PANI electrode. [36] This illustrates that the WTSS scaffold with porous 3D honeycomb structure is beneficial for the electrochemical performance because it acts as electrolyte reservoir. The higher capacitance of the carbon fiber cloth-based RGO/PANI electrode may be attributed to the good conductivity of the carbon-fiber scaffold and the active nanocomposite material RGO/PANI.

4. CONCLUSIONS

We employed an extremely simple dipping-and-drying method to prepare an interesting electrode material consisting of RGO-coated WTSS, and fabricated a solid-state supercapacitor using PVA/H$_3$PO$_4$ gel that functioned simultaneously as electrolyte and separator. WTSS acted as flexible and lightweight substrate with unique porous 3D honeycomb structure and hydrophilic characteristics. These particular properties give the RGO-coated WTSS electrode an excellent areal capacitance of 102 mF cm^{-2} at a low sweep rate of 1 mV s^{-1} and high cyclic stability with 98.9% retention of the initial capacitance after 5000 cycles. The fabricated flexible WTSS-RGO supercapacitor cell also had a high areal power density of 0.47 mW cm^{-2} and exhibited high mechanical flexibility. Maybe this electrode does not achieve the best possible design and performance; however, our present work provides an interesting, new, and more natural candidate material for future energy-storage devices.

REFERENCES

1. J. Liu, C. Yang, H. Wu, Z. Lin, Z. Zhang, R. Wang, B. Li, F. Kang, L. Shi, and C. P. Wong, *Energy Environ. Sci.* **11**, 3674 (2014).
2. Q. Cheng, Z. Song, T. Ma, B. B. Smith, R. Tang, H. Yu, H. Jiang, and C. K. Chan, *Nano Lett.* **13**, 4969 (2013).
3. A. Määttänen, P. Ihalainen, P. Pulkkinen, S. Wang, H. Tenhu, and J. Peltonen, *ACS Appl. Mater. Interfaces* **4**, 955 (2012).
4. L. Hu, J. W. Choi, Y. Yang, S. Jeong, F. La Mantia, L.-F. Cui, and Y. Cui, *PNAS* **106**, 21490 (2009).
5. G. Zheng, L. Hu, H. Wu, X. Xie, and Y. Cui, *Energy Environ. Sci.* **4**, 3368 (2011).
6. A. Razaq, L. Nyholm, M. Sjödin, M. Strømme, and A. Mihranyan, *Adv. Energy Mater.* **2**, 445 (2012).
7. J.-X. Feng, Q. Li, X.-F. Lu, Y.-X. Tong, and G.-R. Li, *J. Mater. Chem. A* **2**, 2985 (2014).
8. L. Yuan, B. Yao, B. Hu, K. Huo, W. Chen, and J. Zhou, *Energy Environ. Sci.* **6**, 470 (2013).
9. Z. Weng, Y. Su, D. W. Wang, F. Li, J. Du, and H. M. Cheng, *Adv. Energy Mater.* **1**, 917 (2011).
10. K. Gao, Z. Shao, J. Li, X. Wang, X. Peng, W. Wang, and F. Wang, *J. Mater. Chem. A* **1**, 63 (2013).
11. Q. Niu, K. Gao, and Z. Shao, *Nanoscale* **6**, 4083 (2014).
12. G. Zheng, Y. Cui, E. Karabulut, L. Wågberg, H. Zhu, and L. Hu, *MRS Bull.* **38**, 320 (2013).
13. Z. Gui, H. Zhu, E. Gillette, X. Han, G. W. Rubloff, L. Hu, and S. B. Lee, *ACS Nano* **7**, 6037 (2013).
14. H. Zhu, Z. Jia, Y. Chen, N. Weadock, J. Wan, O. Vaaland, X. Han, T. Li, and L. Hu, *Nano Lett.* **13**, 3093 (2013).
15. D. N.-S. Hon and N. Shiraishi, *Wood and Cellulosic Chemistry, Revised, and Expanded*, p. 43, CRC Press, Boca Raton (2000).
16. A. K. Geim, *Science* **324**, 1530 (2009).
17. R. Shmulsky and P. D. Jones, *Forest Products and Wood Science*, p. 55, John Wiley & Sons, Hoboken (2011).
18. W. S. Hummers Jr. and R. E. Offeman, *J. Am. Chem. Soc.* **80**, 1339 (1958).
19. V. C. Tung, M. J. Allen, Y. Yang, and R. B. Kaner, *Nat. Nanotechnol.* **4**, 25 (2008).
20. S. He, L. Lin, F. Fu, Y. Zhou, and M. Fan, *BioResources* **9**, 1924 (2014).
21. H. C. Schniepp, J.-L. Li, M. J. McAllister, H. Sai, M. Herrera-Alonso, D. H. Adamson, R. K. Prud'homme, R. Car, D. A. Saville, and I. A. Aksay, *J. Phys. Chem. B* **110**, 8535 (2006).
22. M. D. Stoller, S. Park, Y. Zhu, J. An, and R. S. Ruoff, *Nano Lett.* **8**, 3498 (2008).
23. S. Stankovich, D. A. Dikin, R. D. Piner, K. A. Kohlhaas, A. Kleinhammes, Y. Jia, Y. Wu, S. T. Nguyen, and R. S. Ruoff, *Carbon* **45**, 1558 (2007).
24. P.-G. Ren, D.-X. Yan, X. Ji, T. Chen, and Z.-M. Li, *Nanotechnology* **22**, 055705 (2011).

25. H.-L. Guo, X.-F. Wang, Q.-Y. Qian, F.-B. Wang, and X.-H. Xia, *ACS Nano* **3**, 2653 (2009).
26. N. D. Luong, N. Pahimanolis, U. Hippi, J. T. Korhonen, J. Ruokolainen, L.-S. Johansson, J.-D. Nam, and J. Seppälä, *J. Mater. Chem.* **21**, 13991 (2011).
27. M. Shateri-Khalilabad and M. E. Yazdanshenas, *Cellulose* **20**, 963 (2013).
28. M. D. Stoller and R. S. Ruoff, *Energy Environ. Sci.* **3**, 1294 (2010).
29. Y.-Y. Horng, Y.-C. Lu, Y.-K. Hsu, C.-C. Chen, L.-C. Chen, and K.-H. Chen, *J. Power Sources* **195**, 4418 (2010).
30. J. J. Yoo, K. Balakrishnan, J. Huang, V. Meunier, B. G. Sumpter, A. Srivastava, M. Conway, A. L. Mohana Reddy, J. Yu, and R. Vajtai, *Nano Lett.* **11**, 1423 (2011).
31. A. Vu, Y. Qian, and A. Stein, *Adv. Energy Mater.* **2**, 1056 (2012).
32. S. Lv, F. Fu, S. Wang, J. Huang, and L. Hu, *RSC Adv.* **5**, 2813 (2015).
33. W. W. Liu, X. B. Yan, J. W. Lang, C. Peng, and Q. J. Xue, *J. Mater. Chem.* **22**, 17245 (2012).
34. B. G. Choi, J. Hong, W. H. Hong, P. T. Hammond, and H. Park, *ACS Nano* **5**, 7205 (2011).
35. Y. Wang, J. Chen, J. Cao, Y. Liu, Y. Zhou, J. H. Ouyang, and D. Jia, *J. Power Sources* **271**, 269 (2014).
36. P. Yu, Y. Li, X. Zhao, L. Wu, and Q. Zhang, *Langmuir* **30**, 5306 (2014).